Paleoceanography and Paleoclimatology

RESEARCH ARTICLE
10.1029/2020PA003965

Key Points:

- Glacial-interglacial change in net export production at East Pacific Site 849 from ~3.35 to 2.0 Ma
- No secular change in net export production in the East Pacific across the Plio-Pleistocene transition
- Net export production on secular timescales regulated by nutrient content of upwelled waters, nutricline dynamics, and iron fertilization

Supporting Information:

- Supporting Information S1
- Data Set S1

Correspondence to:
K. A. Jakob,
kim.jakob@geow.uni-heidelberg.de

Citation:
Jakob, K. A., Ho, S. L., Meckler, A. N., Pross, J., Fiebig, J., Keppler, F., & Friedrich, O. (2021). Stable biological production in the eastern equatorial Pacific across the Plio-Pleistocene transition (~3.35–2.0 Ma). *Paleoceanography and Paleoclimatology*, *36*, e2020PA003965. https://doi.org/10.1029/2020PA003965

Received 24 APR 2020
Accepted 2 MAR 2021

Stable Biological Production in the Eastern Equatorial Pacific Across the Plio-Pleistocene Transition (~3.35–2.0 Ma)

Kim A. Jakob[1], S. Ling Ho[2,3], A. Nele Meckler[3], Jörg Pross[1], Jens Fiebig[4], Frank Keppler[1,5], and Oliver Friedrich[1]

[1]Institute of Earth Sciences, Heidelberg University, Heidelberg, Germany, [2]Institute of Oceanography, National Taiwan University, Taipei, Taiwan, [3]Bjerknes Centre for Climate Research and Department of Earth Science, University of Bergen, Bergen, Norway, [4]Institute of Geosciences, Goethe-University Frankfurt, Frankfurt, Germany, [5]Heidelberg Center for the Environment (HCE), Heidelberg University, Heidelberg, Germany

Abstract Upwelling within the Eastern Equatorial Pacific (EEP) Ocean is a key factor for the Earth's climate because it supports >10% of the present-day biological production. The dynamics of upwelling in the EEP across the Plio-Pleistocene transition—an interval particularly relevant for understanding near-future warming due to Anthropocene-like atmospheric carbon-dioxide levels—have been intensively studied for the region east of the East Pacific Rise. In contrast, changes of the equatorial upwelling regime in the open Pacific Ocean west of this oceanographic barrier have received markedly less attention. We therefore provide new proxy records from Ocean Drilling Program Site 849 located within the EEP open-ocean upwelling regime. Our target interval (~3.35–2.0 Ma) covers the Plio-Pleistocene transition characterized by the intensification of Northern Hemisphere Glaciation (iNHG). We use benthic $\delta^{18}O$ values to generate a new, high-resolution age model for Site 849, and sand-accumulation rates together with benthic $\delta^{13}C$ values to evaluate net export production. Although showing temporary substantial glacial-interglacial variations, our records indicate stability in net export production on secular timescales across the iNHG. We suggest the following processes to have controlled the long-term evolution of primary productivity at Site 849. First, nutrient export from the high latitudes to the EEP; second, a successive shoaling of the Pacific nutricline during the studied interval; and third, a simultaneous reduction in dust-borne iron input.

1. Introduction

Oceanic upwelling systems are important for the Earth's atmospheric and marine carbon budget (Toggweiler & Sarmiento, 1985; Watson & Naveira Garabato, 2006). In upwelling regions, relatively cold, nutrient-rich and carbon-dioxide-(CO_2) bearing waters from below the thermocline typically characterize the surface-water hydrography. Such conditions allow for enhanced marine primary productivity and, thus, removal of the upwelled CO_2 from the surface-ocean through organic-matter export into the deep sea. The efficiency of this so-called biological pump is of particular importance in the Eastern Equatorial Pacific (EEP) where coastal and equatorial upwelling support >10% of the biological production in the present-day oceans (Pennington et al., 2006). Across the Plio-Pleistocene transition—a time interval that is highly relevant for the understanding of anthropogenic warming because it comprises climatic boundary conditions and atmospheric CO_2 levels as they are expected in the near future (e.g., Dowsett et al., 2013; Martinez-Boti et al., 2015; Robinson et al., 2008)—major shifts in marine export production occurred in the global oceans (Lawrence et al., 2013, and references therein). However, modes and drivers of these changes within the EEP upwelling regime are not entirely clear.

Since the early Pliocene, the Earth underwent a transition from a warmer climate state and Anthropocene-like atmospheric CO_2 (>400 parts per million by volume [ppmv]) lacking large ice sheets in the Northern Hemisphere to a progressively cooler climate state and pre-industrial-like atmospheric CO_2 (<280 ppmv) during the Pleistocene with a stronger response of the climate/cryosphere system to orbital forcing (Lisiecki & Raymo, 2005; Martinez-Boti et al., 2015; Seki et al., 2010). Over the past ~5 Myr and thus this transitional period, a close coupling between biological production and sea-surface temperatures in the equatorial upwelling system of the East Pacific Ocean has been documented on glacial-interglacial

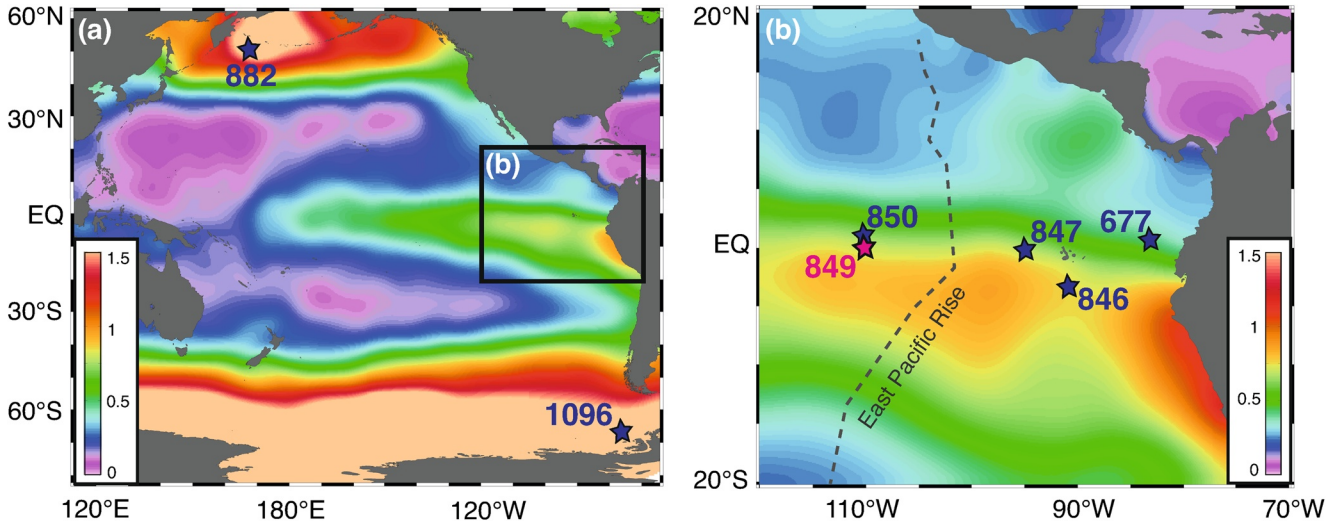

Figure 1. Locations of ODP Site 849 (red; this study) and other sites mentioned in the text (dark blue; previously published data sets) against a background map of modern annual sea-surface phosphate concentrations (in μmol l^{-1}) after World Ocean Atlas 2013 (Garcia et al., 2014) for (a), the Pacific and Southern Oceans and (b) the East Pacific Ocean. Regions with high sea-surface phosphate concentrations (and thus high nutrient availability) are typically associated with high rates of biological production.

(~41-kyr) timescales for Ocean Drilling Program (ODP) Site 846 (Lawrence et al., 2006, Figure 1). Such a coupling suggests changes in thermocline depth and, perhaps, upwelling intensity to have been the main driver for primary productivity (Lawrence et al., 2006; Ma et al., 2015). The amount of nutrients within the upwelled water mass, however, may have acted as an additional controlling factor on glacial-interglacial timescales (Etourneau et al., 2013; Jakob et al., 2016). In contrast, a decoupling between sea-surface temperature and biological production at ODP Sites 846 and 847, both located east of the East Pacific Rise (Figure 1), has been proposed for longer, million-year timescales (Dekens et al., 2007; Farrell et al., 1995; Lawrence et al., 2006). This decoupling points to nutrient availability in upwelled waters as the dominant driver for biological production on secular timescales (Dekens et al., 2007; Lawrence et al., 2006).

To date, investigations on EEP export production are mainly based on study sites located east of the East Pacific Rise. However, these sites could also be affected by local oceanographic factors (such as coastal upwelling) or continental influences (e.g., Ma et al., 2015, and references therein). In contrast, sites west of the East Pacific Rise are representative of equatorial upwelling in the open Pacific Ocean only (Mix et al., 1995; Pisias et al., 1995). Available studies on export production during the Plio-Pleistocene from this region, however, (i) either focus on glacial-interglacial changes across a relatively short time window (<400 kyr; Jakob et al., 2016), (ii) are inconsistent (see opal production records from Lyle et al., 2019 vs. Ma et al., 2015), (iii) or describe single components of oceanic productivity such as barite-/opal- (Ma et al., 2015) or calcium-carbonate ($CaCO_3$) production (Lyle et al., 2019), rather than focusing on net export production.

To shed new light on both the glacial-interglacial and long-term variability in net export production within the equatorial upwelling system of the open Pacific Ocean, we here present new proxy records for ODP Site 849 located in the heart of equatorial upwelling west of the East Pacific Rise (Figure 1). Our target interval is the Plio-Pleistocene transition. Specifically, we focus on the ~3.35 to 2.0 Ma time period (Marine Isotope Stages [MIS] MG1–77). This interval includes three different phases: First, weak-amplitude glacial-interglacial variations of the relatively warm late Pliocene with the exception of a pronounced positive excursion in benthic $\delta^{18}O$ corresponding to the MIS M2 glaciation (~3.3 Ma). Second, the Plio-Pleistocene transition with the culmination of the intensification of Northern Hemisphere Glaciation (iNHG) from MIS 100 to 96 (~2.5 Ma) characterized by the first strong glacial-interglacial cycles. Third, early Pleistocene glacials MIS 82 (~2.15 Ma) and MIS 78 (~2.05 Ma) that are even stronger than the strongest glacials of the iNHG (Lisiecki & Raymo, 2005; for details see Section 4.1).

We use benthic foraminiferal $\delta^{13}C$ values and sand-accumulation rates (SAR) to evaluate net export production during the ~3.35 to 2.0 Ma interval at Site 849. Sand-accumulation rates are well suited to trace net

export production at our study site as the sand fraction (>63 μm) is mainly composed of material from biogenic activity, including both carbonate- and opal-producing organisms (for details see Section 2.2). We further compare our records with additional productivity and climate proxy records from the EEP (e.g., Dekens et al., 2007; Ford et al., 2012; Lawrence et al., 2006; Ma et al., 2015) and elsewhere (e.g., Haug et al., 1999; Hillenbrand & Fütterer, 2001; Lawrence et al., 2013; Studer et al., 2012) to evaluate our findings in a wider geographical context and to investigate the processes that underlie export production at the study site. The suborbital resolution (~700 years) of our records further required refinement of the previously available age model for Site 849 (Mix et al., 1995), which was achieved by tuning our new benthic foraminiferal $\delta^{18}O$ record to the LR04 stack (Lisiecki & Raymo, 2005).

2. Materials and Methods

2.1. Study Site

To generate a continuous record of net export production in the equatorial Pacific upwelling system for the time interval from ~3.35 to 2.0 Ma, we investigated samples from ODP Leg 138 Site 849 (0°11′N, 110°31′W, water depth: 3,851 m; Mayer et al., 1992). Site 849 is located ~860 km west of the East Pacific Rise within the heart of the equatorial upwelling zone in the open Pacific Ocean. The site exhibits continuous sedimentation with sedimentation rates of 2.5–3 cm kyr^{-1} (Jakob et al., 2017; Mayer et al., 1992; Mix et al., 1995) and a $CaCO_3$ content of up to 90% (Lyle et al., 2019) across the targeted interval. The present-day water depth at Site 849 is below the modern lysocline (3,200–3,400 m water depth; Adelseck & Anderson, 1978; Berger et al., 1982), but above the carbonate compensation depth throughout the past 34 Ma (Pälike et al., 2012). Thus, $CaCO_3$ is well-preserved at that site. Good carbonate preservation during the investigated time interval is also indicated by (i) a relatively low planktic foraminiferal fragmentation index (Jakob et al., 2016), which is a proxy for carbonate dissolution (Metzler et al., 1982), and (ii) a good overall preservation of planktic foraminiferal tests shown by scanning electron microscopy (Jakob et al., 2016, 2018). This allows geochemical studies based on well-preserved foraminifera.

2.2. Sample Material

To obtain sedimentological and geochemical information for Site 849, 1,632 samples with a volume of 20 cm^3 were investigated at 2-cm intervals along the primary shipboard splice (Mayer et al., 1992) from Cores 849C-6H-2-70 cm to 849C-6H-3–28 cm, 849C-7H-1-80 cm to 849C-7H-1–150 cm, 849C-8H-1-80 cm to 849C-8H-2–98 cm, 849C-9H-1-46 cm to 849C-9H-3–18 cm, 849D-5H-5-56 cm to 849D-6H-7–24 cm, and 849D-7H-1-21 cm to 849D-8H-6–96 cm (57.02–92.77 m composite depth [mcd]). In addition, ten out-of-splice samples from Core 849C-7H-2 (1–21 cm) corresponding to 70.47–70.65 mcd were investigated, which replaces the splice interval from Core 849D-7H-1 (1–20 cm). The latter was not used because of substantial sediment disturbances (Mayer et al., 1992). Together, this yields a total of 1,642 samples.

The sample material was dried, weighed and washed over a 63 μm sieve. The >63 μm residue (sand fraction) consists mainly of calcareous planktic and benthic foraminifera, together with siliceous radiolarians and diatoms, and therefore is ideally suited to trace net export production (see Section 4.2).

2.3. Determination of Sand-Accumulation Rates

We generated a new record of SAR for the studied interval of Site 849 except for the interval corresponding to ~2.75–2.4 Ma, for which such data already exist (Jakob et al., 2016, 2018). Following the approach described in Jakob et al. (2016), SAR was calculated based on linear sedimentation rates (LSRs) as derived from our new age model (see Section 3.1), dry bulk density (DBD) data as calculated from high-resolution density shipboard measurements through Gamma Ray Attenuation Porosity Evaluation (GRAPE; IODP JANUS database; Mayer et al., 1992) and the portion of the >63 μm sand fraction per gram dry sediment (SF, weights determined during sample processing) as $SAR = LSR \times DBD \times SF$.

2.4. Stable-Isotope Analysis

$\delta^{18}O$ and $\delta^{13}C$ records were generated based on the benthic foraminiferal species *Oridorsalis umbonatus*, although $\delta^{18}O$ values derived from the benthic foraminifer *Cibicidoides wuellerstorfi* are more commonly used for age-model determination (e.g., Bolton et al., 2010; Lawrence et al., 2006). High-resolution records for Site 849 based on *C. wuellerstorfi* are also already available for the ~2.75–2.4 Ma interval (Jakob et al., 2016, 2017), and low-resolution (sampling interval: 10–20 cm) *C. wuellerstorfi*-derived $\delta^{18}O$ and $\delta^{13}C$ records exist for the entire investigated time interval (Mix et al., 1995). However, we decided to not extend these records because of the following reasons: First, Site 849 samples investigated in this study comprise more tests of *O. umbonatus* than of *C. wuellerstorfi* continuously throughout the record. Second, *O. umbonatus* also yields the possibility to carry out further geochemical analysis (such as Mg/Ca) on the same material. This is because *O. umbonatus* has fewer and larger chambers than *C. wuellerstorfi*, facilitating proper cleaning of tests for further geochemical analysis. Moreover, the shallow infaunal habitat of *O. umbonatus* implies that this species is well buffered from the carbonate-ion effect (Rathmann & Kuhnert, 2008) and therefore better suited as a Mg/Ca recorder than the epifaunal species *C. wuellerstorfi*.

To generate benthic foraminiferal $\delta^{18}O$ and $\delta^{13}C$ records, on average twelve *O. umbonatus* tests were picked per sample from the >150 μm fraction. Subsequently, tests were cracked, homogenized, and a subsample of ~1/3 was used for stable-isotope analysis. Samples were analyzed using a Thermo Fisher Scientific 253 Plus isotope ratio mass spectrometer coupled to a Thermo Fisher Scientific Kiel IV Carbonate Device (both Thermo Fisher Scientific, Bremen, Germany) at Heidelberg University and a MAT253 gas source mass spectrometer equipped with a Gas Bench II (Thermo Quest Finnigan, Bremen, Germany) at Goethe University Frankfurt (for details see Data Set S1). All $^{13}C/^{12}C$ and $^{18}O/^{16}O$ isotope ratios are expressed in the conventional δ notation in per mil versus Vienna Pee Dee Belemnite (VPDB). At Heidelberg University, an in-house carbonate standard (Solnhofen limestone) calibrated against the reference material IAEA-603 (calcite; $\delta^{13}C_{VPDB} = +2.46 \pm 0.01‰$ and $\delta^{18}O_{VPDB} = -2.37 \pm 0.04‰$) was used to normalize all measured raw $\delta^{13}C$ and $\delta^{18}O$ values to the VPDB isotope reference scale; samples were processed following an in-house protocol. At Goethe University Frankfurt, $\delta^{13}C$ and $\delta^{18}O$ values are reported relative to the VPDB standard through the analysis of in-house standard (Carrara marble) calibrated to NBS-19 (limestone; $\delta^{13}C_{VPDB} = +1.95‰$ and $\delta^{18}O_{VPDB} = -2.20‰$, exactly) and NBS-18 (carbonatite; $\delta^{13}C_{VPDB} = -5.06‰$ and $\delta^{18}O_{VPDB} = -23.01‰$, exactly); samples were processed according to the protocol outlined by Spötl and Vennemann (2003). External precisions for $\delta^{13}C$ and $\delta^{18}O$ values are better than 0.02 and 0.06‰ (at 1σ level) for samples analyzed at Heidelberg University using the Kiel IV, and <0.1‰ (at 1σ level) for the samples measured at Goethe University Frankfurt using the Gas Bench II, respectively. Replicate measurements of sample material show that $\delta^{13}C$ and $\delta^{18}O$ values derived from both laboratories are indistinguishable within this analytical precision.

2.5. Chronology

For the past 5 Myr, an age model for Site 849 is already available (Mix et al., 1995). It is based on correlations between (i) benthic foraminiferal (*C. wuellerstorfi*) $\delta^{18}O$ records of Site 849 and ODP Site 677 (Figure 1) for the 2.5–0 Ma interval, and (ii) Site 849 GRAPE-density data and orbital insolation for the 5–2.5 Ma time period. However, this age model is limited by the relatively low temporal resolution of its underlying $\delta^{18}O$ data set (10–20 cm; Mix et al., 1995) and the additional uncertainty associated with the combination of different stratigraphic methods.

In the recent past, the alignment of benthic $\delta^{18}O$ records to the LR04 stack has emerged as a common strategy to achieve age information for deep-sea sediment cores (Lisiecki & Raymo, 2005). Based on this approach, a high-resolution chronology is already available for Site 849 for the 77.02–67.78 mcd interval, corresponding to ~2.75–2.4 Ma in the time domain (Jakob et al., 2016, 2017). This age model is based on a $\delta^{18}O$ record of the benthic species *C. wuellerstorfi*. We used this age model, and generated a new one for the remainder of the investigated time interval (i.e., ~3.35–2.75 Ma and ~2.4–2.0 Ma), based on the benthic species *O. umbonatus* (for details see Table S1). The good overall agreement of $\delta^{18}O$ records from *O. umbonatus* and *C. wuellerstorfi* from Site 849 shows that this is a reliable approach (see Figure S1).

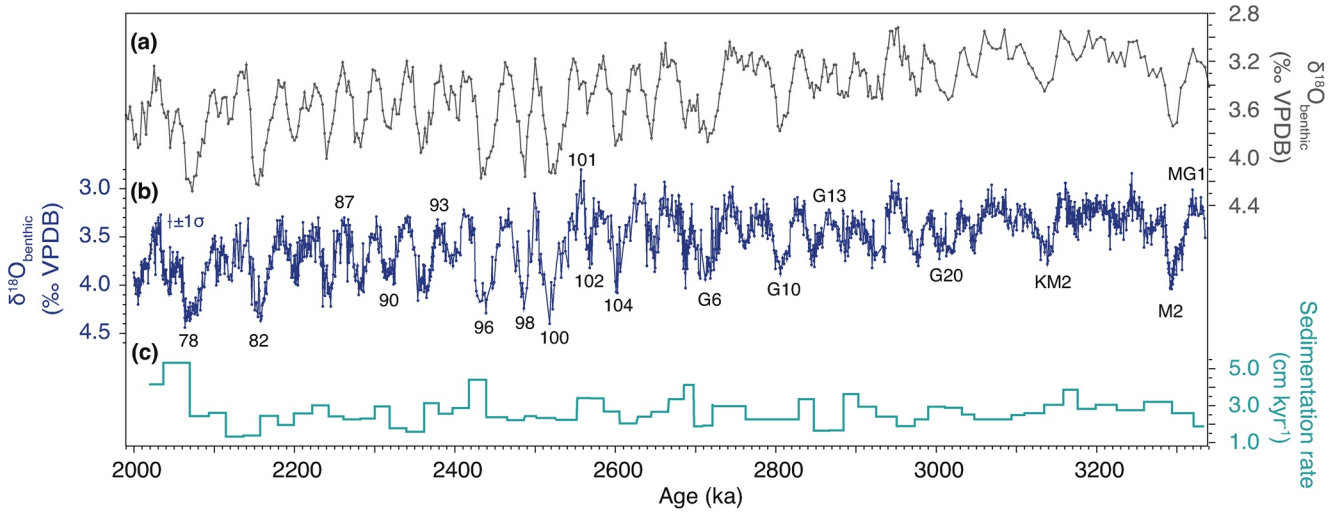

Figure 2. New age model for ODP Site 849 for ~3.35–2.0 Ma (MIS MG1–77). (a) Global benthic foraminiferal $\delta^{18}O$ record (LR04 stack; Lisiecki & Raymo, 2005). (b) Benthic foraminiferal $\delta^{18}O$ record from Site 849 tuned to the LR04 stack; horizontal and vertical bars indicate the 1σ standard deviation. (c) Sedimentation rates for Site 849. Tie points for tuning are provided in Table S1. Selected MIS are labeled for reference.

The new age model for Site 849 (Figure 2) was constructed via visual correlation of the benthic $\delta^{18}O$ record to the LR04 stack (Lisiecki & Raymo, 2005) using the AnalySeries software package version 2.0.8 (Paillard et al., 1996). To minimize errors during tuning (Bolton et al., 2010) and to remain consistent with the already available age model for the ~2.75–2.4 Ma interval (Jakob et al., 2016, 2017), only one tie point at the midpoint of each glacial-interglacial transition was used (for details see Table S1).

2.6. Trend Analysis, Evolutionary Spectral Analysis and Cross-Spectral Analysis

To identify secular trends for the ~3.35–2.0 Ma time interval in proxy records generated for and used in this study, linear regressions were applied to the individual data sets and the ~3.35–2.0 Ma time span. Results (Table S2) are indicated as dashed lines in the respective figures.

The temporal evolution of periodicities in the records was identified by applying wavelet analysis to evenly-spaced data using the software PAleontological STatistics (PAST version 3.11; Hammer et al., 2001) and the Morlet wavelet as the mother wavelet. Furthermore, we quantified coherencies and phase lags between records through Blackman-Tukey cross-spectral analysis with 30% overlap using the AnalySeries software package version 2.0.8 (Paillard et al., 1996). The data used for cross-spectral analysis were linearly interpolated, detrended, and pre-whitened. Note that our study only focusses on obliquity (41-kyr) cycles even though additional cycles are obviously present.

3. Results

3.1. Chronology

The new chronology for Site 849 yields an average sedimentation rate of 2.9 cm kyr^{-1} and a mean temporal sample resolution of ~700 years (corresponding to 2-cm intervals in the depth domain) for the ~3.35–2.0 Ma period (MIS MG1–77). These results are in agreement with sedimentation rates of 2.5–3.0 cm kyr^{-1} as derived from the previously available age model for the same site and time interval (Mix et al., 1995; see Figure S2). Maximum and minimum sedimentation rates that we reconstruct are 5.3 and 1.3 cm kyr^{-1}, respectively (Figure 2c). Although the highest sedimentation rates are associated with the strong glacials of MIS 96 and 78, a glacial-interglacial cyclicity is generally lacking in the sedimentation rates of Site 849.

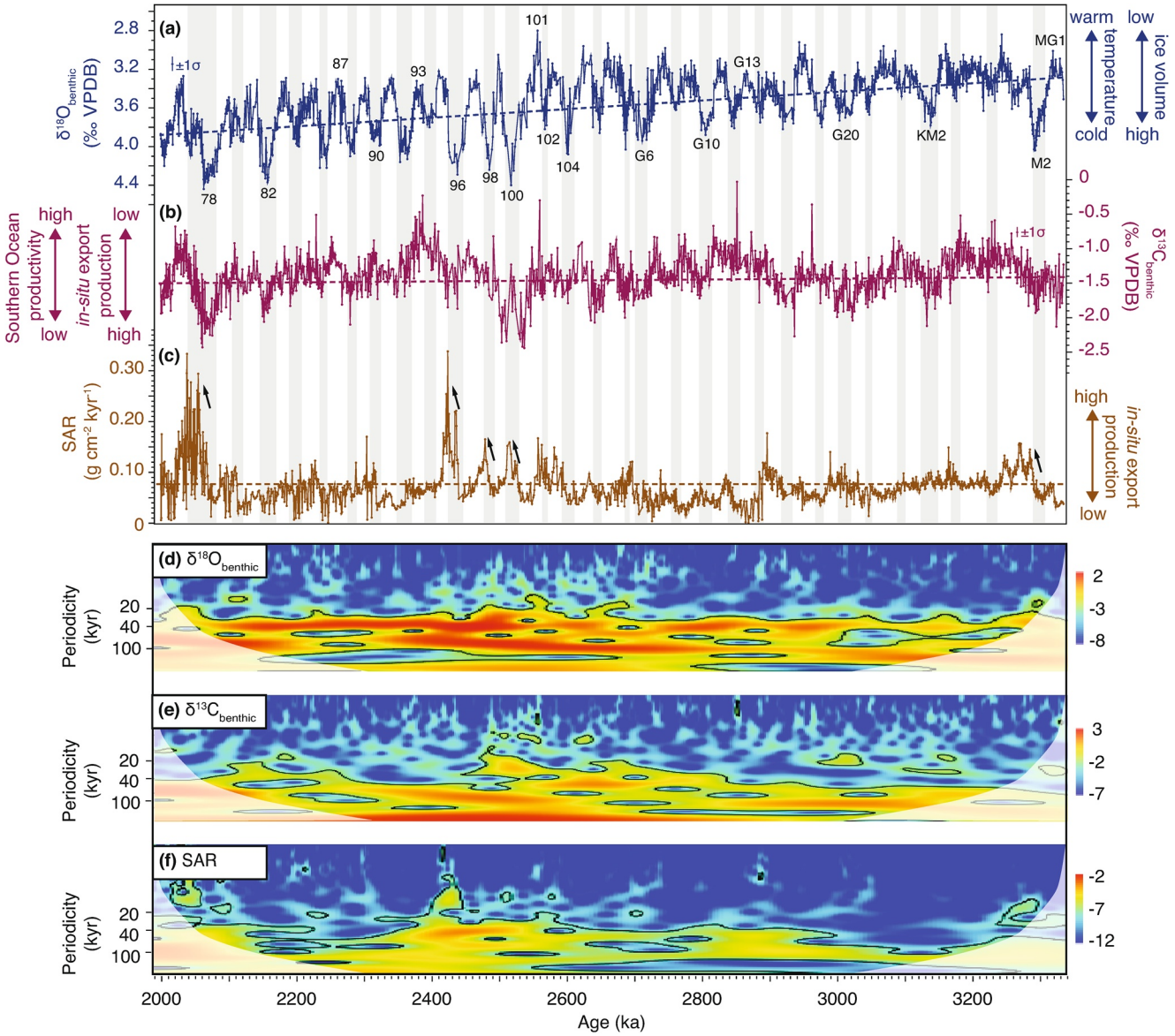

Figure 3. Productivity proxy records for Site 849 for the ~3.35–2.0 Ma interval and evolutionary spectra. (a) Benthic foraminiferal $\delta^{18}O$ record for reference. (b) Benthic foraminiferal $\delta^{13}C$ record; high (low) values indicate a mixed signature of low (high) rates of in situ export production but at the same time high (low) rates of primary productivity in EEP source waters (for details see Section 4.2). Horizontal and vertical bars in a and b indicate the 1σ standard deviation associated with the individual records. (c) Sand-accumulation rates; high (low) values indicate high (low) rates of in situ export production (for details see Section 4.2). Dashed lines in a–c indicate long-term trends and gray bars mark glacial periods; selected MIS are labeled for reference. (d–f) Wavelet analysis for benthic $\delta^{18}O$, benthic $\delta^{13}C$ and SAR. Black lines indicate the 95% significance levels; white shading marks the cone of influence, that is the region in which record length might not be sufficient to interpret results.

3.2. Stable-Isotope Records and Sand-Accumulation Rates

In general, our new *O. umbonatus*-based $\delta^{18}O$ record captures the pattern as derived from the LR04 stack (Lisiecki & Raymo, 2005) and the previously available, lower-resolved $\delta^{18}O$ record (*C. wuellerstorfi*) from the same site and time interval (Mix et al., 1995; see Figure S1). However, due to its higher temporal resolution our record provides a much more detailed picture of the evolution of deep-sea $\delta^{18}O$ values throughout the studied time interval. It varies between 2.80‰ reached during MIS 101 (~2.56 Ma) and 4.44‰ associated with MIS 78 (~2.06 Ma) (Figure 3a), showing a clear glacial-interglacial cyclicity paced by Earth's obliquity with lowest (highest) values corresponding to interglacials (glacials) (Figure 3d). The amplitude of the glacial-interglacial change becomes progressively stronger from MIS 100 onwards. We also observe a clear

long-term trend in our benthic $\delta^{18}O$ data, with an increase in average $\delta^{18}O$ values by ~0.5‰ from ~3.35 to ~2.0 Ma (Figure 3a; see also Table S2). For the ~2.75–2.4 Ma interval, the pattern derived from our new $\delta^{18}O$ record is identical to the already available high-resolution *C. wuellerstorfi*-based $\delta^{18}O$ record from the same site (Jakob et al., 2016, 2017; see Figure S1).

The $\delta^{13}C$ values of *O. umbonatus* range from a minimum of −2.44‰ during MIS 100 (~2.54 Ma) to a maximum of −0.23‰ during MIS 93 (~2.39 Ma), disregarding the apparent outliers at ~2.23, ~2.56, ~2.86, and ~2.96 Ma (Figure 3b). Visual evaluation of the $\delta^{13}C$ record suggests that lowest (highest) values are typically associated with full glacial (interglacial) conditions, and evolutionary spectral analysis indicates that variations in $\delta^{13}C$ are paced by Earth's obliquity (Figure 3e). In contrast to the $\delta^{18}O$ record, there is no long-term trend in the $\delta^{13}C$ record (Figure 3b; see also Table S2). The overall pattern and glacial-interglacial amplitudes are similar to the previously available, lower-resolved $\delta^{13}C$ record (*C. wuellerstorfi*) from the same site and time interval (Mix et al., 1995) and the high-resolution $\delta^{13}C$ record (*C. wuellerstorfi*) for the ~2.65–2.4 Ma interval (Jakob et al., 2016; see Figure S3).

The SAR record yields minimum values of 0.001 g cm^{-2} kyr^{-1} and maximum values of 0.338 g cm^{-2} kyr^{-1} reached during interglacials MIS G13 and 87 (~2.87 and ~2.25 Ma), i.e., when benthic $\delta^{18}O$ values are low, and glacials MIS 96 and 78 (~2.42 and ~2.06 Ma), i.e., when benthic $\delta^{18}O$ values are high, respectively (Figure 3c). Evolutionary spectral analysis indicates a 41-kyr glacial-interglacial cyclicity in this record (Figure 3f). Visually, the glacial-interglacial cyclicity can be observed particularly for those glacial-interglacial cycles comprising the strong glacials of MIS M2, 100–96 and 78 (Figure 4). Lowest values typically occur toward the end of each interglacial-to-glacial transition, followed by progressively increasing values starting at peak glacials and culminating at glacial terminations. Cross-spectral analysis indicates that the Site 849 SAR record lags the benthic $\delta^{18}O$ record by ~7.5–17 kyr for the 41-kyr glacial-interglacial period (Figure 4; see also Figure S4). This finding is consistent with previous observations from the same site for the MIS 100–96 interval (Jakob et al., 2016). Similar to the evolution of $\delta^{13}C$ values, no long-term trend in SAR values emerges over the course of the record (Figure 3c; see also Table S2).

4. Discussion

4.1. Climatic Background Conditions as Derived from $\delta^{18}O$ Values of Site 849

The benthic foraminiferal $\delta^{18}O$ signature is an important recorder for climate evolution. It is a function of temperature and seawater $\delta^{18}O$. The latter, in turn, is controlled by ice volume and precipitation/evaporation, hence salinity. Because the deep ocean is relatively uniform with regard to salinity, benthic foraminiferal $\delta^{18}O$ values are typically used as a measure for relative global ice-volume and deep-ocean temperature variability (e.g., Emiliani, 1955; Lisiecki & Raymo, 2005; Shackleton, 1967; Urey, 1947; Zachos et al., 2001).

In light of the above, low $\delta^{18}O$ values of the late Pliocene represent a relatively warm climate state that was only interrupted by an intense glacial period at ~3.3 Ma (i.e., MIS M2) with $\delta^{18}O$ values characteristic of latest Pliocene glacials MIS G10 or G6 (Figure 3a). Quantitative ice-volume estimates for MIS M2, however, remain uncertain. For instance, Tan et al. (2017) suggest an increase of global ice volume by 16 m relative to the present-day, including 4 and 12 m contributions from the Southern and the Northern Hemispheres, respectively. These estimates fall into the lower range of sea-level lowstand reconstructions for MIS M2 of ~10–65 m below modern (Miller et al., 2020, and references therein). The occurrence of ice-rafted debris in the Arctic Ocean, Nordic Seas and the North Atlantic (De Schepper et al., 2014, and references therein) provides evidence for the presence of ice in the Northern Hemisphere. Glacial MIS M2 has been consequently inferred as an early attempt of Earth's climate to establish intense, frequently waxing and waning Northern Hemisphere ice sheets (De Schepper et al., 2013, and references therein) as they finally emerged only ~500 kyr later. The time interval comprising these changes toward the build-up of larger ice sheets in the Northern Hemisphere together with global cooling is typically considered to span ~3.6–2.4 Ma (Mudelsee & Raymo, 2005) and widely termed iNHG.

The iNHG can be traced by progressively increasing $\delta^{18}O$ values over the course of our record (Figure 3a; see also Table S2). The final phase of iNHG (MIS 100–96) is also clearly expressed in our data set by (i) an increase in glacial $\delta^{18}O$ values from on average ~3.8‰ (MIS M2–102) to ~4.4‰ (MIS 100–96) and (ii) amplified glacial-interglacial variations. Both marine and terrestrial geological records indicate that during these

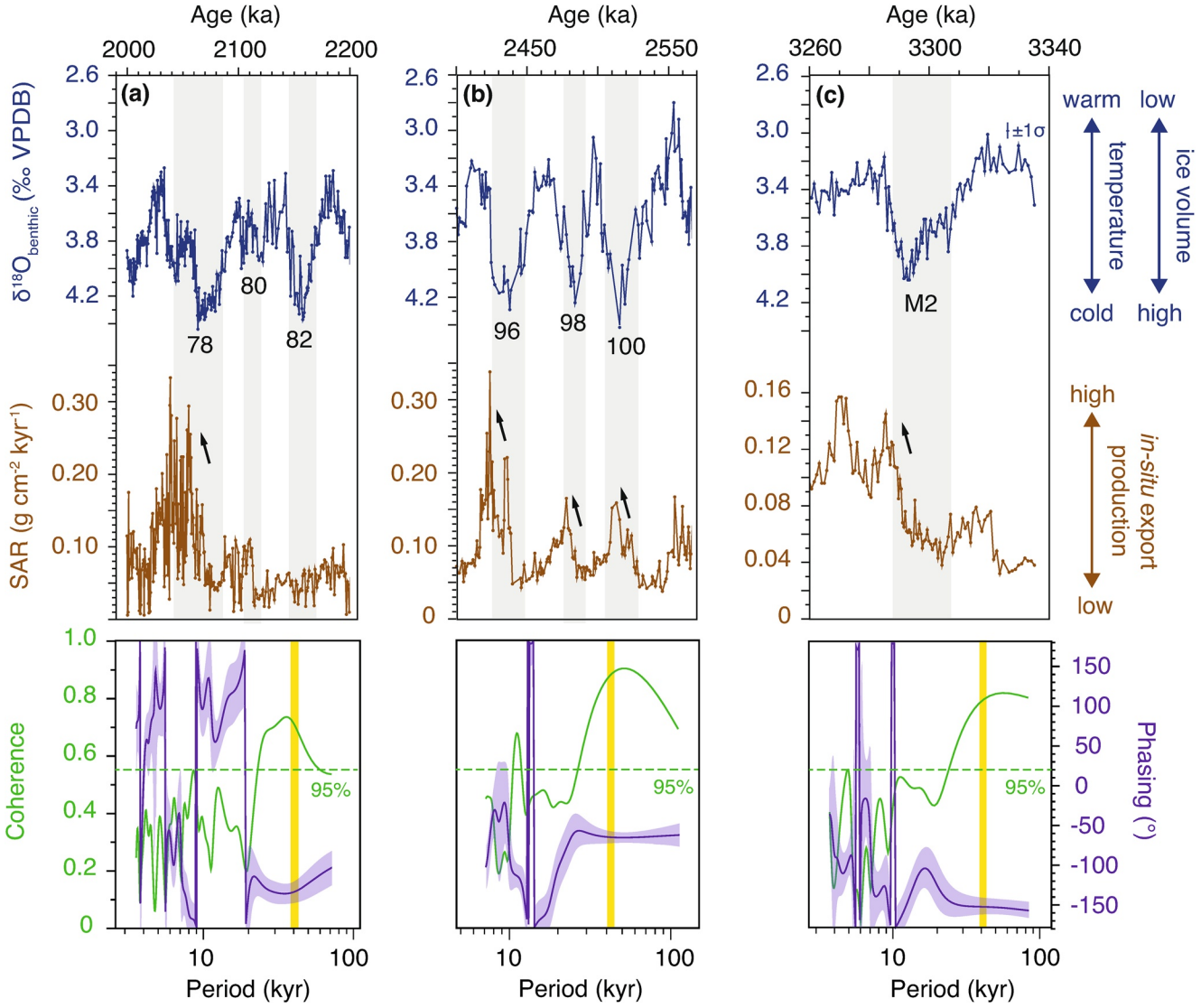

Figure 4. Glacial-interglacial cyclicity in Site 849 benthic $\delta^{18}O$ and export production (upper panel) and phase relationship between these two records (lower panel) for three different time windows. (a) MIS 83–77 (~2.2–2.0 Ma). (b) MIS 101–97 (~2.55–2.40 Ma). (c) MIS MG1–M1 (~3.34–3.26 Ma). The benthic foraminiferal $\delta^{18}O$ record is shown in blue; low (high) values indicate relatively warm (cold) deep-sea temperatures and/or a small (large) ice volume; horizontal and vertical bars indicate the 1σ standard deviation. Sand-accumulation rates are indicated in brown; high (low) values indicate high (low) rates of in situ export production (for details see Section 4.2). Arrows mark the increase in SAR at glacial-interglacial transitions. Gray bars mark glacial periods and glacials are labeled for reference. The lower panel shows coherence (green) and phase relationship (purple) between benthic $\delta^{18}O$ and productivity (SAR) for the individual time intervals at the 95% confidence level (dashed line), determined by Blackman-Tukey cross-spectral analysis. Phasing indicates that productivity (SAR) lags benthic $\delta^{18}O$ for the 41-kyr period (yellow bar) by ~−135 ± 14°, −66.5 ± 7.5° and −152 ± 10.5° (equal to ~−15 ± 1.5 kyr, −7.5 ± 1 kyr and −17 ± 1 kyr) for the ~2.2–2.0 Ma, the ~2.55–2.40 Ma and the ~3.34–3.26 Ma interval, respectively.

prominent glacials of the iNHG sea level dropped to ~40–70 m below modern (de Boer et al., 2014; Jakob et al., 2020), the Laurentide Ice Sheet advanced into the mid-latitudes, and large-scale ice rafting occurred across the North Atlantic Ocean for the first time (Bailey et al., 2010; Balco & Rovey, 2010; Shackleton et al., 1984). In our record, the high $\delta^{18}O$ values of glacials MIS 100–96 are reached again during glacials MIS 82 and 78. The latter glacials are possibly associated with strong ice build-up in the Northern Hemisphere as evidenced by ice-rafted debris in the North Atlantic Ocean (Raymo et al., 1986) and a sea-level lowering of up to ~60 m below modern (Miller et al., 2020).

In general, the above described pattern of our new benthic $\delta^{18}O$ record captures the overall pattern as derived from the global benthic LR04 stack (Lisiecki & Raymo, 2005; see Figure S1). Importantly, this lends

further support to the general assumption of benthic $\delta^{18}O$ values at Site 849 reflecting a quasi-global signal without strong local or terrestrial imprints due to its position west of the East Pacific Rise in the open Pacific Ocean (Mix et al., 1995; Pisias et al., 1995).

4.2. Primary Productivity in the Eastern Equatorial Pacific

The $\delta^{13}C$ signature of benthic foraminiferal tests is routinely used as a tracer for the efficiency of the biological pump (e.g., Kroopnick, 1985; Mackensen & Bickert, 1999; Zahn et al., 1986). A more (less) efficient biological pump can thereby typically be traced with low (high) benthic $\delta^{13}C$ values. However, previous work on Site 849 has shown that the interpretation of foraminiferal $\delta^{13}C$ values is more complicated, suggesting that the benthic $\delta^{13}C$ signal here does not simply trace in situ changes in the strength of the biological pump (Jakob et al., 2016). This assumption is based on parallel trends in planktic and benthic $\delta^{13}C$ records at Site 849 for the ~2.65–2.4 Ma interval that cannot easily be reconciled with benthic $\delta^{13}C$ representing in situ primary production; in such a scenario, benthic $\delta^{13}C$ should instead run inverse to the planktic $\delta^{13}C$ signal. The in situ benthic $\delta^{13}C$ signal is thus rather overprinted by the $\delta^{13}C$ signature of source waters that mainly originate from the Southern Ocean, which, in turn, strongly depends on biological production in that region. Higher (lower) benthic $\delta^{13}C$ values at EEP Site 849 are thereby associated with enhanced (reduced) biological production in the Southern Ocean (Jakob et al., 2016). To trace in situ primary productivity changes at Site 849, a second, independent proxy is thus required.

As shown previously (Diester-Haass et al., 2002; Jakob et al., 2016), the rate of sand (>63 μm) accumulation is a valuable tracer for net export production if the following prerequisites are met: (i) The sand fraction is predominantly composed of material produced by biogenic activity, and (ii) other controlling factors on SAR such as $CaCO_3$ dissolution or the strength of bottom-water currents can be excluded. The redistribution of sand-sized particles by relatively slow bottom-water currents is unlikely at Site 849, and also foraminiferal fragmentation does not indicate carbonate dissolution at the studied site and time interval (for details see Jakob et al., 2016, and references therein). Because sand-sized particles at Site 849 are mainly composed of calcareous and siliceous biogenic material, SAR can thus be used as a proxy for net ocean productivity: Lower (higher) values thereby indicate reduced (enhanced) primary productivity in surface waters (Jakob et al., 2016).

4.2.1. Glacial-Interglacial Variability

In light of the above, our high (low) benthic $\delta^{13}C$ data (Figure 3b) document enhanced (suppressed) primary productivity in Southern Ocean surface waters during interglacials (glacials), likely being related to less sea-ice coverage during interglacials than glacials (Jakob et al., 2016, and references therein). At the same time, enhanced (suppressed) primary productivity in the Southern Ocean might restrict (increase) biological production in the EEP during full interglacial (glacial) conditions via controlling the nutrient delivery to low-latitude upwelling regions.

This tentative interpretation of glacial-interglacial $\delta^{13}C$ variations in terms of in situ production at Site 849 (see Section 4.2) can only partly be supported by our SAR record, which confirms the previous observation (Jakob et al., 2016) that Site 849 $\delta^{13}C$ values do not only depend on in situ primary productivity. This is because the timing of glacial-interglacial change in the $\delta^{13}C$ and SAR records is offset. More precisely, in contrast to the $\delta^{13}C$ record in which peak values are associated with full (inter-)glacial conditions, our SAR record reveals net productivity levels increasing from full glacial conditions and peaking at glacial-interglacial transitions. This pattern particularly emerges during strong (as evidenced by $\delta^{18}O$ values; Figure 3a) glacial-interglacial cycles covering MIS M2, 100–96 and 78 (Figure 4).

Enhanced glacial biological activity during the ~3.0–1.5 Ma period (including MIS 100–96 and 78) also occurs at Site 846 as derived from a record of C_{37} alkenone mass accumulation (Lawrence et al., 2006, 2013). However, highest productivity levels here are reached during peak glacial conditions, leading SAR at Site 849 by approximately one-fourth of the obliquity cycle (Figures 5 and 6a). The picture derived from Site 847 $CaCO_3$ mass-accumulation rates is slightly different (Farrell et al., 1995). Despite its lower temporal resolution compared to Site 849 SAR, visual inspection of that record indicates a higher overall variability, but a weaker glacial-interglacial (41-kyr) signal (Figure 6b). Nevertheless, enhanced biological ($CaCO_3$)

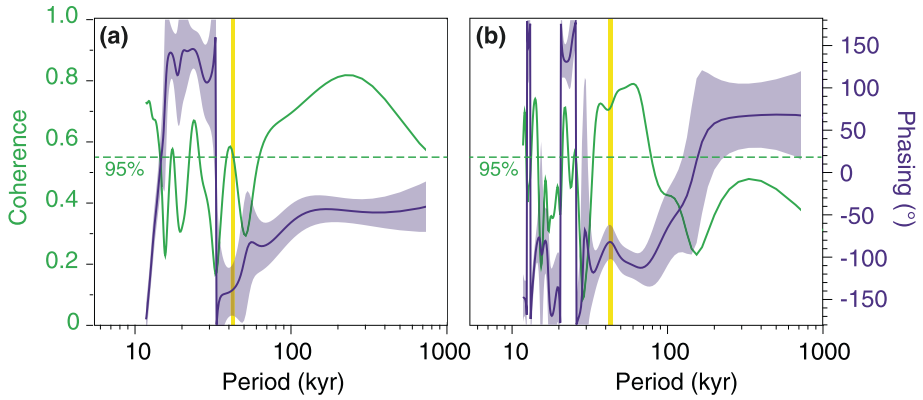

Figure 5. Blackman-Tukey cross-spectral analysis for the identification of coherencies and phasing between productivity proxy records from EEP Sites 846 and 849. Coherence (green) and phase relationship (purple) between SAR (Site 849, this study) and C_{37} alkenone mass-accumulation rates (Site 846, Lawrence et al., 2006, 2013) at the 95% confidence level (dashed line) for (a) the 2.4–2.0 Ma interval and (b) the 3.0–2.4 Ma interval. Values in the phase plots of −140 ± 29° and −90 ± 20° for the 2.4–2.0 Ma and 3.0–2.4 Ma intervals, respectively, indicate that Site 849 SAR is lagging the productivity proxy record from Site 846 by ~16 ± 3 kyr and ~10 ± 2 kyr for the 41-kyr period (yellow bar). Note that cross-spectral analysis was performed using original age models for Sites 846 (Lawrence et al., 2006) and 849 (this study), which are practically identical as they are based on a correlation of benthic $\delta^{18}O$ to LR04 (Lisiecki & Raymo, 2005); therefore results derived from the cross-spectral analysis are robust.

production (i) during peak glacial conditions of MIS 96, as observed for Site 846, and (ii) during glacial-interglacial transitions following MIS 98 and 78, as observed for Site 849, also emerges at Site 847.

Interestingly, net export production as derived from our SAR record appears to have remained low across MIS 82 at Site 849 (Figure 6c). At least in terms of $\delta^{18}O$ values, however, this glacial was as strong as the glacials of MIS M2 or MIS 100–96 (Figure 3a). Thus, a similar positive excursion in primary productivity would be expected. Mass-accumulation rates of biogenic opal support our observation (Figure 6d), indicating low biological production at Site 849 during the early Pleistocene, including MIS 82, that did not increase prior to MIS 78 (Lyle et al., 2019). In contrast, alkenone accumulation at Site 846 suggests enhanced primary productivity for peak glacial conditions of MIS 82, but shows low biological production across MIS M2 (Figure 6a; Lawrence et al., 2006, 2013); the latter is also inferred for Site 847 (Figure 6b; Farrell et al., 1995).

The above-described partially inconsistent pattern in strength and timing of biological production for sites west (Site 849) and east (Sites 846 and 847) of the East Pacific Rise suggests at least temporary different environmental processes or nutrient sources (e.g., coastal vs. equatorial upwelling, continental input) as a driver for biological production on glacial-interglacial timescales and therefore support previous observations (Jakob et al., 2016; Ma et al., 2015). However, despite these differences, proxy records from regions west and east of the East Pacific Rise all show a coupling between local upper-ocean temperature and biological production on glacial-interglacial timescales (Lawrence et al., 2006; Ma et al., 2015), which appears to be of particular relevance during glacial-interglacial cycles with strong glacials (see Figure S5). This points to thermocline depth/upwelling strength as the dominant driver for productivity variations at least over these strong glacial-interglacial cycles in the EEP.

4.2.2. Long-Term Variations in Primary Productivity in the Eastern Equatorial Pacific

For Site 849 we find no secular change in our productivity proxy record across the studied interval (Figure 3c; see also Table S2). This observation is supported by other, lower-resolution records on opal and carbonate production (Figure 6d and 6e) from the same site (Lyle et al., 2019). However, our finding is not consistent with export-production estimates derived from a lower-resolution barite-accumulation record for Site 849 (Ma et al., 2015), which suggests a clear decrease in biological activity from ~3.35 to 2.0 Ma (Figure 6f). Because barite accumulation is typically associated with the accumulation of opal (Murray et al., 2012), its pattern should be similar, if not identical, to opal deposition at the same site (Lyle et al., 2019). Considering that this is not the case for Site 849 (compare Figure 6d and 6f), a plausible explanation for this discrepancy is that barite accumulation may have been influenced by factors other than biological production, such as

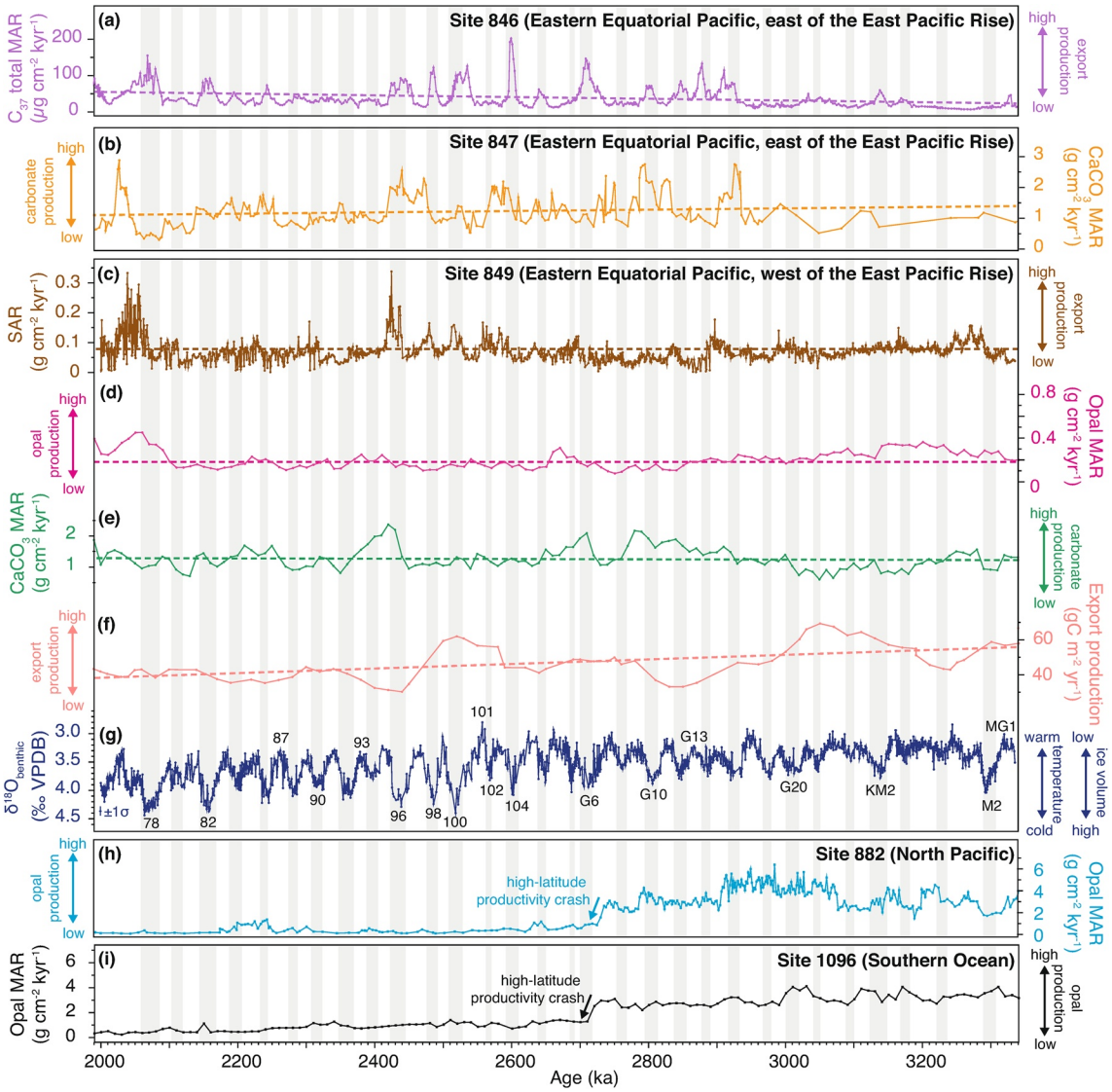

Figure 6. Productivity proxy records for the ~3.35–2.0 Ma interval. (a) C_{37} alkenone mass-accumulation rates at East Pacific Site 846 (Lawrence et al., 2006, 2013). (b) $CaCO_3$-accumulation rates at East Pacific Site 847 (Farrell et al., 1995). (c) Sand-accumulation rates at East Pacific Site 849 (this study). (d) Opal-accumulation rates at Site 849 (Lyle et al., 2019). (e) $CaCO_3$-accumulation rates at Site 849 (Lyle et al., 2019). (f) Export production at Site 849 derived from barite accumulation (Ma et al., 2015). Dashed lines in (a–f) depict long-term trends in the proxy records. (g) Benthic foraminiferal $\delta^{18}O$ record at Site 849 for reference (this study); horizontal and vertical bars indicate the 1σ standard deviation. (h) Opal-accumulation rates at North Pacific Site 882 (Haug et al., 1999). (i) Opal-accumulation rates at Southern Ocean Site 1096 (Hillenbrand & Fütterer, 2001). Gray bars mark glacial periods; selected MIS are labeled for reference.

sediment focusing or terrestrial influence (Paytan & Griffith, 2007; Paytan et al., 2004). Supporting evidence for such a scenario comes from neighboring ODP Site 850 (Figure 1), for which no statistically significant correlation between barium and other productivity indicators over the past 4 Myr is registered (Schroeder et al., 1997).

We conclude that long-term net-export-production rates at Site 849 remained stable throughout the studied interval. This observation is consistent with the previously available productivity proxy records from Sites 846 (Lawrence et al., 2006, 2013) and 847 (Dekens et al., 2007; Farrell et al., 1995) that reveal no or only a minor trend for the ~3.35–2.0 Ma interval—a finding that is largely unaffected by increased productivity associated with strong glacials since ~3.0 Ma (Figure 6a and 6b). Importantly, as trend analysis for all records is only performed for the ~3.35–2.0 Ma period to allow for a more direct comparison to our new Site

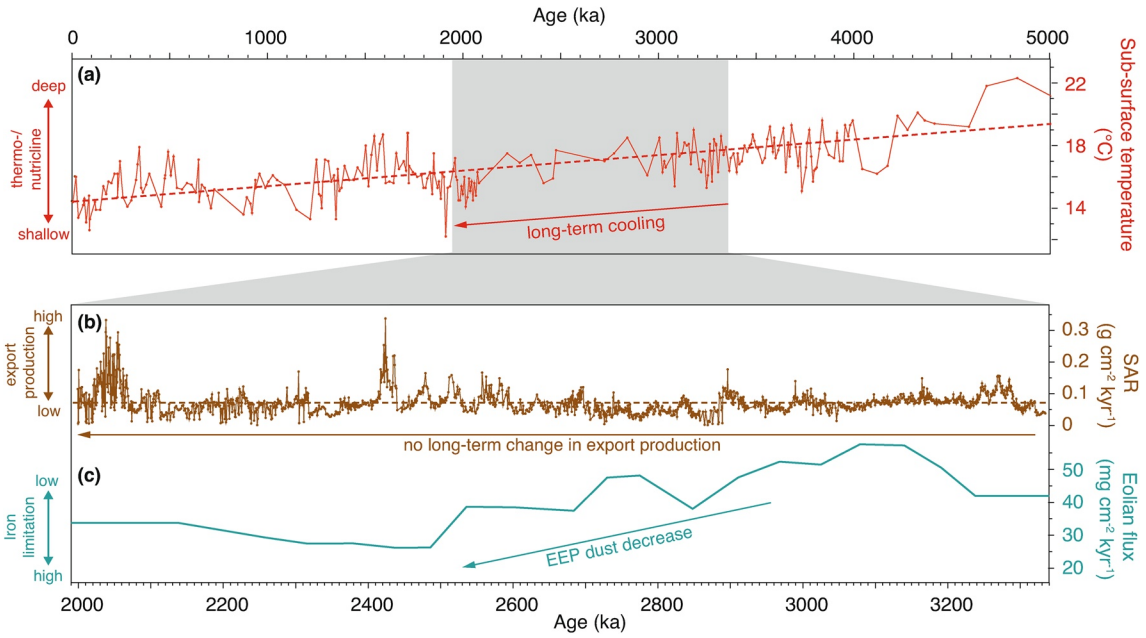

Figure 7. Controlling environmental processes of long-term productivity changes at Site 849 during the ~3.35–2.0 Ma interval. (a) Sub-surface temperature evolution at Site 849 for the past 5 Myr (Ford et al., 2012). (b) Sand-accumulation rates as a proxy for export production at EEP Site 849 (this study). Dashed lines in a and b, illustrate long-term trends. (c) Eolian flux data for Site 849 (Hovan, 1995).

849 records, results might differ from what has been observed in previous studies for timescales longer than our study interval.

Assuming Site 849 records an open-ocean signal due to its position west of the East Pacific Rise, the agreement in the long-term signal of available records from Sites 846, 847 and 849 for ~3.35–2.0 Ma indicates that the influence from continents (e.g., via river input) and/or of local oceanography (e.g., coastal upwelling) was negligible at sites east of the East Pacific Rise on secular timescales. However, considering that the Earth's climate crossed a major tipping point during our study interval, the iNHG, a major shift in biological production as observed elsewhere (e.g., in the North Pacific (Haug et al., 1999, Figure 6h), the Southern Ocean (Hillenbrand & Fütterer, 2001, Figure 6i), or the equatorial Atlantic (Lawrence et al., 2013)) would be expected (for details see Section 4.2.2.2). Therefore, we next evaluate the underlying processes that might have suppressed changes in biological production in the EEP.

4.2.2.1. Primary Productivity and Upwelling Strength

The cooling of surface waters and, at the same time, increasing productivity within these waters is typically invoked to result from thermocline shoaling/stronger upwelling. However, proxy records from the equatorial upwelling region east of the East Pacific Rise (Sites 846 and 847) appear to not support this coupling during the past ~5 Myr for secular timescales (Dekens et al., 2007; Lawrence et al., 2006). To identify whether this pattern also emerges at Site 849 (which we consider representative for the equatorial upwelling system in the open Pacific Ocean; see Section 4.1), we next provide a comparison between our new productivity proxy record and long-term upper-ocean temperature evolution at the studied site.

At Site 849, a long-term cooling of ~2°C from ~3.35 to 2.0 Ma is documented by a Mg/Ca-derived temperature record of sub-surface waters (Figure 7a; Ford et al., 2012). In contrast to this temperature record, our record on net export production shows no secular change from ~3.35 to 2.0 Ma (Figure 7b). There are two possibilities to explain this observation. First, primary productivity at Site 849 was indeed decoupled from upper-ocean temperature/upwelling strength on secular timescales as suggested in previous studies (Dekens et al., 2007; Lawrence et al., 2006). Second, upwelling strength and productivity were not decoupled but another factor counteracted upwelling-related changes in biological production—an avenue that we will focus on in the following section.

4.2.2.2. Controlling Factors for Primary Productivity in the Eastern Equatorial Pacific

Previous studies have suggested that secular changes in primary productivity in the EEP were controlled by the nutrient supply within the upwelled water mass rather than by upwelling strength (Dekens et al., 2007; Lawrence et al., 2006). Waters upwelled in the EEP are typically considered to derive from Subantarctic Mode Water, which originates from the Southern Ocean (Sarmiento et al., 2004; Toggweiler et al., 1991; Tsuchiya et al., 1989), but contributions from the North Pacific through North Pacific Intermediate Water may also be of importance (Sarmiento et al., 2004).

Productivity proxy records from EEP source waters, i.e., the Southern Ocean (ODP Site 1096; Hillenbrand & Fütterer, 2001) and the North Pacific (ODP Site 882; Haug et al., 1999; Sigman et al., 2004) (Figures 1, Figure 6h and 6i), indicate an abrupt, prominent decrease in primary productivity at ~2.7 Ma associated with the iNHG. This polar productivity crash likely resulted from an equatorward migration of westerly winds, which shifted the locus of Ekman divergence and therefore upwelling of nutrient-enriched waters in both hemispheres gradually toward lower latitudes. At the same time, nutrient supply to polar surface waters became restricted due to water-column stratification (Haug et al., 1999; Lawrence et al., 2013; Sigman et al., 2004). The latter is supported by evidence from nitrogen isotopes for increased relative nutrient utilization in these polar waters since ~2.7 Ma (McKay et al., 2012; Studer et al., 2012).

While the zone of high-latitude upwelling and productivity migrated equatorwards, the locus of downwelling, i.e., the source region of nutrients to be exported to the lower latitudes, also shifted toward the equator (Lawrence et al., 2013). The time-transgressive high-latitude productivity decrease thus does not necessarily affect the amount of nutrients transported to the EEP and therefore productivity rates there. However, the equatorward shift in the locus of up-/downwelling likely also led to a successive contraction of the tropical warm pool and a shoaling of the tropical nutri-/thermocline (Lawrence et al., 2013)—possibly a result of upwelling intensification—which culminated in the development of the EEP cold tongue between ~1.8 and 1.2 Ma (Martínez-Garcia et al., 2010). Although the rate of nutrients exported from the high latitudes might have remained unchanged, nutricline shoaling would lead to a higher amount of nutrients that are available in the photic zone and thus increased biological activity. This, however, conflicts our observation of no long-term trend in EEP productivity rates from both sites west and east of the East Pacific Rise over the ~3.35–2.0 Ma period (Figures 6a–6e). There are two possibilities to explain this inconsistency. First, nutricline shoaling in the EEP was not strong enough to have a significant effect on biological production within the photic zone for which, perhaps, a specific threshold value (in terms of nutricline depth) needs to be crossed. Second, a counterbalancing factor acted to promote rather constant productivity rates on secular timescales in the entire EEP.

In this context, iron limitation might play a role as it controls the amount of biological production in the EEP today (Coale et al., 1996; Martínez-García & Winckler, 2014). Important natural sources of iron for ocean fertilization are eolian dust and upwelling of ocean waters (Winckler et al., 2008, 2016). The iron supply in upwelled waters should behave similar to its nutrient content and, assuming nutricline shoaling across the studied interval, should further support a long-term productivity increase. However, dust-borne iron input to the EEP appears to have decreased from ~3.1 to ~2.4 Ma according to the eolian flux data from Site 849 (Figure 7c; Hovan, 1995). This reduction in eolian flux is connected to wetter conditions in continental source regions (i.e., central and northern South America) in response to a southward migration of the Intertropical Convergence Zone associated with Northern Hemisphere cooling and ice-sheet growth (Hovan, 1995). A reduced dust input at Site 849 might thus have counterbalanced the simultaneous shoaling of the tropical nutricline across the iNHG. Together, these processes likely promoted a stable productivity level in the EEP on secular timescales.

5. Conclusions

We have integrated new and previously published sedimentological and geochemical records from ODP Site 849 to reconstruct net export production in the equatorial upwelling system of the open East Pacific Ocean across the Plio-Pleistocene transition (~3.35–2.0 Ma, MIS MG1–77). Our data document glacial-interglacial variations in net export production at Site 849 that are different in timing to other EEP sites, possibly implying a heterogeneous behavior of the equatorial upwelling system east and west to the East Pacific

Rise. Importantly, this discrepancy does not exist on secular timescales from ~3.35 to 2.0 Ma, for which we observe a rather constant productivity level at different sites all over the EEP. For these timescales we identified the interplay of (i) nutrient export from the high latitudes to the EEP, (ii) nutricline dynamics in the tropics, and (iii) dust-derived iron input into the EEP to have controlled biological production in the East Pacific, although the latter factors (nutricline dynamics and iron fertilization) likely acted to cancel each other out. Ultimately, our study adds to a growing body of work on the environmental processes that affect nutrient availability and primary productivity during warmer-than-modern climates.

Data Availability Statement

The data associated with this study are available in the supporting information and on Zenodo (https://doi.org/10.5281/zenodo.4431601).

Acknowledgments
This research used samples provided by the Ocean Drilling Program (ODP). ODP was sponsored by the U.S. National Science Foundation (NSF) and participating countries under the management of Joint Oceanographic Institutions (JOI), Inc. Philipp Geppert, Lena Heiler, Franz Kerschhofer, Verena Schreiber (all Heidelberg University) and Jordan Donn-Holl (University of Bergen) helped with sample processing. Sven Hofmann (University of Frankfurt), Markus Greule and Bernd Knape (both Heidelberg University) are thanked for their support in stable-isotope analysis. Funding for this study was provided by the German Research Foundation (DFG, grants JA2803/2–1 to Kim Alix Jakob, FR2544/6 to Oliver Friedrich and PR651/15 to Jörg Pross) and the Trond Mohn Foundation (grant BFS2015REK01) to Sze Ling Ho and Anna Nele Meckler. Open Access funding enabled and organized by Projekt DEAL.

References

Adelseck, C. G., & Anderson, T. F. (1978). The late Pleistocene record of productivity fluctuations in the eastern equatorial Pacific Ocean. *Geology*, *6*, 388–391. https://doi.org/10.1130/0091-7613(1978)6<388:tlprop>2.0.co;2

Bailey, I., Bolton, C. T., DeConto, R. M., Pollard, D., Schiebel, R., & Wilson, P. A. (2010). A low threshold for North Atlantic ice rafting from "low-slung slippery" late Pliocene ice sheets. *Journal of Geophysical Research*, *25*, PA1212. https://doi.org/10.1029/2009PA001736

Balco, G., & Rovey, C. W. (2010). Absolute chronology for major Pleistocene advances of the Laurentide Ice Sheet. *Geology*, *38*(9), 795–798. https://doi.org/10.1130/g30946.1

Berger, W. H., Bonneau, M.-C., & Parker, F. L. (1982). Foraminifera on the deep-sea floor: lysocline and dissolution rate. *Oceanologica Acta*, *5*, 249–258.

Bolton, C. T., Wilson, P. A., Bailey, I., Friedrich, O., Beer, C. J., Becker, J., et al. (2010). Millennial-scale climate variability in the subpolar North Atlantic Ocean during the late Pliocene. *Journal of Geophysical Research*, *25*, PA4218. https://doi.org/10.1029/2010PA001951

Coale, K. H., Johnson, K. S., Fitzwater, S. E., Gordon, R. M., Tanner, S., Chavez, F. P., et al. (1996). A massive phytoplankton bloom induced by an ecosystem-scale iron fertilization experiment in the equatorial Pacific Ocean. *Nature*, *383*, 495–501. https://doi.org/10.1038/383495a0

de Boer, B., Lourens, L. J., & van de Wal, R. S. W. (2014). Persistent 400,000-year variability of Antarctic ice volume and the carbon cycle is revealed throughout the Plio-Pleistocene. *Nature Communications*, *5*. https://doi.org/10.1038/ncomms3999

Dekens, P. S., Ravelo, A. C., & McCarthy, M. D. (2007). Warm upwelling regions in the Pliocene warm period. *Journal of Geophysical Research*, *22*, A3211. https://doi.org/10.1029/2006PA001394

De Schepper, S., Gibbard, P. L., Salzmann, U., & Ehlers, J. (2014). A global synthesis of the marine and terrestrial evidence for glaciation during the Pliocene Epoch. *Earth-Science Reviews*, *135*, 83–102. https://doi.org/10.1016/j.earscirev.2014.04.003

De Schepper, S., Groeneveld, J., Naafs, B. D. A., Van Renterghem, C., Hennissen, J., Head, M. J., et al. (2013). Northern hemisphere glaciation during the globally warm early Late Pliocene. *PLoS ONE*, *8*(12), e81508. https://doi.org/10.1371/journal.pone.0081508

Diester-Haass, L., Meyers, P. A., & Vidal, L. (2002). The late Miocene onset of high productivity in the Benguela Current upwelling system as part of a global pattern. *Marine Geology*, *180*, 87–103. https://doi.org/10.1016/s0025-3227(01)00207-9

Dowsett, H. J., Foley, K. M., Stoll, D. K., Chandler, M. A., Sohl, L. E., Bentsen, M., et al. (2013). Sea surface temperature of the mid-Piacenzian ocean: A data-model comparison. *Scientific Reports*, *3*. https://doi.org/10.1038/srep02013

Emiliani, C. (1955). Pleistocene temperatures. *The Journal of Geology*, *63*, 538–578. https://doi.org/10.1086/626295

Etourneau, J., Robinson, R. S., Martinez, P., & Schneider, R. (2013). Equatorial Pacific peak in biological production regulated by nutrient and upwelling during the late Pliocene/early Pleistocene cooling. *Biogeosciences*, *10*(8), 5663–5670. https://doi.org/10.5194/bg-10-5663-2013

Farrell, J. W., Raffi, I., Janecek, T. R., Murray, D. W., Levitan, M., Dadey, K. A., et al. (1995). *Late Neogene sedimentation patterns in the eastern equatorial Pacific Ocean*. In N. G. Pisias, L. A. Mayer, T. R. Janecek, A. Palmer-Julson, & T. H. van Andel, (Eds.), Proceedings of the Ocean Drilling Program, Scientific Results (Vol. 138, pp. 717–756). College Station, TX: Ocean Drilling Program.

Ford, H. L., Ravelo, A. C., & Hovan, S. (2012). A deep Eastern Equatorial Pacific thermocline during the early Pliocene warm period. *Earth and Planetary Science Letters*, *355–356*, 152–161. https://doi.org/10.1016/j.epsl.2012.08.027

Garcia, H. E., Locarnini, R. A., Boyer, T. P., Antonov, J. I., Baranova, O. K., Zweng, M. M., et al. (2014). *Dissolved Inorganic Nutrients (phosphate, nitrate, silicate)*. In S. Levitus, (Ed.), World Ocean Atlas 2013 (Vol. 4, p. 25). Washington, DC: Government Printing Office.

Hammer, Ø., Harper, D. A. T., & Ryan, P. D. (2001). Past: Paleontological statistics software package for education and data analysis. *Palaeontologia Electronica*, *4*(1). http://palaeo-electronica.org/2001_1/past/issue1_01.htm

Haug, G. H., Sigman, D. M., Tiedemann, R., Pedersen, T. F., & Sarnthein, M. (1999). Onset of permanent stratification in the subarctic Pacific Ocean. *Nature*, *401*, 779–782. https://doi.org/10.1038/44550

Hillenbrand, C.-D., & Fütterer, D. K. (2001). *Neogene to Quaternary deposition of opal on the continental rise west of the Antarctic Peninsula, ODP Leg 178, Sites 1095, 1096, and 1101*. In P. F. Barker, A. Camerlenghi, G. D. Acton, & A. T. S. Ramsay, (Eds.), Proceedings of the Ocean Drilling Program, Scientific Results (Vol. 178, pp. 1–33). College Station, TX: Ocean Drilling Program

Hovan, S. A. (1995). *Late Cenozoic atmospheric circulation intensity and climatic history recorded by eolian deposition in the eastern equatorial Pacific Ocean, Leg 138*. In N. G. Pisias, L. A. Mayer, T. R. Janecek, A. Palmer-Julson, & T. H. van Adel, (Eds.), Proceedings of the Ocean Drilling Program, Scientific Results (Vol. 138, pp. 615–625). College Station, TX: Ocean Drilling Program.

Jakob, K. A., Bolton, C. T., Wilson, P. A., Bahr, A., Pross, J., Fiebig, J., et al. (2017). Glacial-interglacial changes in equatorial Pacific surface-water structure during the Plio-Pleistocene intensification of Northern Hemisphere Glaciation. *Earth and Planetary Science Letters*, *463*, 69–80. https://doi.org/10.1016/j.epsl.2017.01.028

Jakob, K. A., Pross, J., Scholz, C., Fiebig, J., & Friedrich, O. (2018). Thermocline state change in the eastern equatorial Pacific during the late Pliocene/early Pleistocene intensification of Northern Hemisphere Glaciation. *Climate of the Past*, *14*(7), 1079–1095. https://doi.org/10.5194/cp-14-1079-2018

Jakob, K. A., Wilson, P. A., Bahr, A., Bolton, C. T., Pross, J., Fiebig, J., & Friedrich, O. (2016). Plio-Pleistocene glacial-interglacial productivity changes in the eastern equatorial Pacific upwelling system. *Journal of Geophysical Research: Paleoceanography*, *31*, 453–470. https://doi.org/10.1002/2015PA002899

Jakob, K. A., Wilson, P. A., Pross, J., Ezard, T. H. G., Fiebig, J., Repschläger, J., & Friedrich, O. (2020). A new sea-level record for the Neogene/Quaternary boundary reveals transition to a more stable East Antarctic Ice Sheet. *Proceedings of the National Academy of Sciences of the United States of America*, *117*, 30980–30987. https://doi.org/10.1073/pnas.2004209117

Kroopnick, P. M. (1985). The distribution of 13C of ΣCO2 in the world oceans. *Deep Sea Research A. Oceanographic Research Papers*, *32*(1), 57–84. https://doi.org/10.1016/0198-0149(85)90017-2

Lawrence, K. T., Liu, Z., & Herbert, T. D. (2006). Evolution of the eastern tropical Pacific through Plio-Pleistocene glaciation. *Science*, *312*, 79–83. https://doi.org/10.1126/science.1120395

Lawrence, K. T., Sigman, D. M., Herbert, T. D., Riihimaki, C. A., Bolton, C. T., Martinez-Garcia, A., et al. (2013). Time-transgressive North Atlantic productivity changes upon Northern Hemisphere glaciation. *Journal of Geophysical Research: Paleoceanography*, *28*, 740–751. https://doi.org/10.1002/2013PA002546

Lisiecki, L. E., & Raymo, M. E. (2005). A Pliocene-Pleistocene stack of 57 globally distributed benthic δ18O records. *Journal of Geophysical Research*, *20*, A1003. https://doi.org/10.1029/2004PA001071

Lyle, M., Drury, A. J., Tian, J., Wilkens, R., & Westerhold, T. (2019). Late Miocene to Holocene high-resolution eastern equatorial Pacific carbonate records: Stratigraphy linked by dissolution and paleoproductivity. *Climate of the Past*, *15*(5), 1715–1739. https://doi.org/10.5194/cp-15-1715-2019

Ma, Z., Ravelo, A. C., Liu, Z., Zhou, L., & Paytan, A. (2015). Export production fluctuations in the eastern equatorial Pacific during the Pliocene-Pleistocene: Reconstruction using barite accumulation rates. *Journal of Geophysical Research: Paleoceanography*, *30*, 1455. https://doi.org/10.1002/2015PA002860

Mackensen, A., & Bickert, T. (1999). Stable carbon isotopes in benthic foraminifera: Proxies for deep and bottom water circulation and new production. In G. Fischer, & G. Wefer, (Eds.), *Use of Proxies in Paleoceanography: Examples from the South Atlantic* (pp. 229–254). Berlin: Springer-Verlag.

Martínez-Botí, M. A., Foster, G. L., Chalk, T. B., Rohling, E. J., Sexton, P. F., Lunt, D. J., et al. (2015). Plio-Pleistocene climate sensitivity evaluated using high-resolution CO_2 records. *Nature*, *518*(7537), 49–54. https://doi.org/10.1038/nature14145

Martínez-Garcia, A., Rosell-Melé, A., McClymont, E. L., Gersonde, R., & Haug, G. H. (2010). Subpolar Link to the emergence of the modern equatorial Pacific cold tongue. *Science*, *328*, 1550–1553. https://doi.org/10.1126/science.1184480

Martínez-García, A., & Winckler, G. (2014). Iron fertilization in the glacial ocean. *PAGES Mag*, *22*(2), 82–83. https://doi.org/10.22498/pages.22.2.82

Mayer, L., Pisias, N., Janecek, T., et al. (1992). Proceedings of the ocean drilling programinitial reports (Vol. 138). College Station, TX: Ocean Drilling Program.

McKay, R., Naish, T., Carter, L., Riesselman, C., Dunbar, R., Sjunneskog, C., et al. (2012). Antarctic and Southern Ocean influences on Late Pliocene global cooling. *Proceedings of the National Academy of Sciences*, *109*(17), 6423–6428. https://doi.org/10.1073/pnas.1112248109

Metzler, C. V., Wenkam, C. R., & Berger, W. H. (1982). Dissolution of foraminifera in the eastern equatorial Pacific; an in situ experiment. *Journal of Foraminiferal Research*, *12*, 362–368. https://doi.org/10.2113/gsjfr.12.4.362

Miller, K. G., Browning, J. V., John Schmelz, W., Kopp, R. E., Mountain, G. S., & Wright, J. D. (2020). Cenozoic sea-level and cryospheric evolution from deep-sea geochemical and continental margin records. *Science Advances*, *6*, eaaz1346. https://doi.org/10.1126/sciadv.aaz1346

Mix, A. C., Pisias, N. G., Rugh, W., Wilson, J., Morey, A., & Hagelberg, T. K. (1995). *Benthic foraminifer stable isotope record from Site 849 (0–5 Ma): Local and global climate changes*. In N. G. Pisias, L. A. Mayer, T. R. Janecek, A. Palmer-Julson, & T. H. van Adel, (Eds.), Proceedings of the Ocean Drilling Program, Scientific Results (Vol. 138, pp. 371–412). College Station, TX: Ocean Drilling Program.

Mudelsee, M., & Raymo, M. E. (2005). Slow dynamics of the Northern Hemisphere Glaciation. *Journal of Geophysical Research*, *20*, PA4022. https://doi.org/10.1029/2005PA001153

Murray, R. W., Leinen, M., & Knowlton, C. W. (2012). Links between iron input and opal deposition in the Pleistocene equatorial Pacific Ocean. *Nature Geoscience*, *5*(4), 270–274. https://doi.org/10.1038/ngeo1422

Paillard, D., Labeyrie, L., & Yiou, P. (1996). Macintosh Program performs time-series analysis. *Eos Transactions AGU*, *77*(39), 379. https://doi.org/10.1029/96EO00259

Pälike, H., Lyle, M. W., Nishi, H., Raffi, I., Ridgwell, A., Gamage, K., et al. (2012). A Cenozoic record of the equatorial Pacific carbonate compensation depth. *Nature*, *488*(7413), 609–614. https://doi.org/10.1038/nature11360

Paytan, A., & Griffith, E. M. (2007). Marine barite: Recorder of variations in ocean export productivity. *Deep Sea Research Part II: Topical Studies in Oceanography*, *54*(5–7), 687–705. https://doi.org/10.1016/j.dsr2.2007.01.007

Paytan, A., Lyle, M., Mix, A., & Chase, Z. (2004). Climatically driven changes in oceanic processes throughout the equatorial Pacific. *Journal of Geophysical Research*, *19*, PA4017. https://doi.org/10.1029/2004PA001024

Pennington, J. T., Mahoney, K. L., Kuwahara, V. S., Kolber, D. D., Calienes, R., & Chavez, F. P. (2006). Primary production in the eastern tropical Pacific: A review. *Progress in Oceanography*, *69*(2–4), 285–317. https://doi.org/10.1016/j.pocean.2006.03.012

Pisias, N. G., Mayer, L. A., & Mix, A. C. (1995). *Paleoceanography of the eastern equatorial Pacific during the Neogene: Synthesis of Leg 138 drilling results*. In N. G. Pisias, L. A. Mayer, T. R. Janecek, A. Palmer-Julson, & T. H. van Adel, (Eds.), Proceedings of the ocean drilling program, scientific results (Vol. 138, pp. 5–21). College Station, TX: Ocean Drilling Program.

Rathmann, S., & Kuhnert, H. (2008). Carbonate ion effect on Mg/Ca, Sr/Ca and stable isotopes on the benthic foraminifera *Oridorsalis umbonatus* off Namibia. *Marine Micropaleontology*, *66*(2), 120–133. https://doi.org/10.1016/j.marmicro.2007.08.001

Raymo, M. E., Ruddiman, W. F., & Clement, B. M. (1986). *Pliocene-Pleistocene paleoceanography of the North Atlantic at Deep Sea Drilling Project Site 609*. In W. F. Ruddiman, R. B. Kidd, E. Thomas, et al., (Eds.), Initial Reports of the. Deep Sea Drilling Project (Vol. 94, pp. 895–901). Washington D.C.: U.S. Governmental Printing Office.

Robinson, M. M., Dowsett, H. J., & Chandler, M. A. (2008). Pliocene role in assessing future climate impacts. *Eos Transactions AGU*, *89*(49), 501–502. https://doi.org/10.1029/2008eo490001

Sarmiento, J. L., Gruber, N., Brzezinski, M. A., & Dunne, J. P. (2004). High-latitude controls of thermocline nutrients and low latitude biological productivity. *Nature*, *427*, 56–60. https://doi.org/10.1038/nature02127

Schroeder, J. O., Murray, R. W., Leinen, M., Pflaum, R. C., & Janecek, T. R. (1997). Barium in equatorial Pacific carbonate sediment: Terrigenous, oxide, and biogenic associations. *Journal of Geophysical Research*, *12*(1), 125–146. https://doi.org/10.1029/96pa02736

Seki, O., Foster, G. L., Schmidt, D. N., Mackensen, A., Kawamura, K., & Pancost, R. D. (2010). Alkenone and boron-based Pliocene pCO_2 records. *Earth and Planetary Science Letters*, *292*(1–2), 201–211. https://doi.org/10.1016/j.epsl.2010.01.037

Shackleton, N. (1967). Oxygen isotope analyses and Pleistocene temperatures re-assessed. *Nature*, *215*, 15–17. https://doi.org/10.1038/215015a0

Shackleton, N. J., Backman, J., Zimmerman, H., Kent, D. V., Hall, M. A., Roberts, D. G., et al. (1984). Oxygen isotope calibration of the onset of ice-rafting and history of glaciation in the North Atlantic region. *Nature*, *307*, 620–623. https://doi.org/10.1038/307620a0

Sigman, D. M., Jaccard, S. L., & Haug, G. H. (2004). Polar ocean stratification in a cold climate. *Nature*, *428*, 59–63. https://doi.org/10.1038/nature02357

Spötl, C., & Vennemann, T. W. (2003). Continuous-flow isotope ratio mass spectrometric analysis of carbonate minerals. *Rapid Communications in Mass Spectrometry*, *17*(9), 1004–1006. https://doi.org/10.1002/rcm.1010

Studer, A. S., Martínez-Garcia, A., Jaccard, S. L., Girault, F. E., Sigman, D. M., & Haug, G. H. (2012). Enhanced stratification and seasonality in the Subarctic Pacific upon Northern Hemisphere Glaciation-New evidence from diatom-bound nitrogen isotopes, alkenones and archeal tetraethers. *Earth and Planetary Science Letters*, *351–352*, 84–94. https://doi.org/10.1016/j.epsl.2012.07.029

Tan, N., Ramstein, G., Dumas, C., Contoux, C., Ladant, J.-B., Sepulchre, P., et al. (2017). Exploring the MIS M2 glaciation occurring during a warm and high atmospheric CO_2 Pliocene background climate. *Earth and Planetary Science Letters*, *472*, 266–276. https://doi.org/10.1016/j.epsl.2017.04.050

Toggweiler, J. R., Dixon, K., & Broecker, W. S. (1991). The Peru upwelling and the ventilation of the south Pacific thermocline. *Journal of Geophysical Research*, *96*, 20467–20497. https://doi.org/10.1029/91jc02063

Toggweiler, J. R., & Sarmiento, J. L. (1985). Glacial to interglacial changes in atmospheric carbon dioxide: the role of ocean surface water in high latitudes. *Geophysical Monograph*, *32*, 163–184.

Tsuchiya, M., Lukas, R., Fine, R. A., Firing, E., & Lindstrom, E. (1989). Source waters of the Pacific Equatorial Undercurrent. *Progress in Oceanography*, *23*, 101–147. https://doi.org/10.1016/0079-6611(89)90012-8

Urey, H. C. (1947). The thermodynamic properties of isotopic substances. *Journal of the Chemical Society*, 562–581. https://doi.org/10.1039/jr9470000562

Watson, A. J., & Naveira Garabato, A. C. (2006). The role of Southern Ocean mixing and upwelling in glacial-interglacial atmospheric CO_2 change. *Tellus B: Chemical and Physical Meteorology*, *58*, 73–87. https://doi.org/10.1111/j.1600-0889.2005.00167.x

Winckler, G., Anderson, R. F., Fleisher, M. Q., McGee, D., & Mahowald, N. (2008). Covariant glacial-interglacial dust fluxes in the equatorial Pacific and Antarctica. *Science*, *320*, 93–96. https://doi.org/10.1126/science.1150595

Winckler, G., Anderson, R. F., Jaccard, S. L., & Marcantonio, F. (2016). Ocean dynamics, not dust, have controlled equatorial Pacific productivity over the past 500,000 years. *Proceedings of the National Academy of Sciences of the United States of America*, *113*(22), 6119–6124. https://doi.org/10.1073/pnas.1600616113

Zachos, J., Pagani, M., Sloan, L., Thomas, E., & Billups, K. (2001). Trends, rhythms, and aberrations in global climate 65 Ma to present. *Science*, *292*, 686–693. https://doi.org/10.1126/science.1059412

Zahn, R., Winn, K., & Sarnthein, M. (1986). Benthic foraminiferal δ13C and accumulation rates of organic carbon: Uvigerina Peregrina group and *Cibicidoides wuellerstorfi*. *Journal of Geophysical Research*, *1*, 27–42. https://doi.org/10.1029/pa001i001p00027